mater.scichina.com link.springer.com

Published online 24 November 2023 | https://doi.org/10.1007/s40843-023-2654-5
Sci China Mater 2023, 66(12): 4587–4594

Co nanoparticles-embedded hierarchical porous carbon network as high-performance cathode for lithium-sulfur batteries

Lichao Fu, Dapeng Liu*, Xintao Zuo, Haohan Yu, Zerui Fu and Yu Zhang*

ABSTRACT Lithium-sulfur batteries (LSBs) are one of the most promising electrochemical energy storage systems because of their great advantages in theoretical energy density. However, poor conductivities of sulfur and discharge products Li_2S_2 and Li_2S, volume expansion during charge/discharge, and the shuttle effect of lithium polysulfides (LiPSs) severely limit the capacity and cycle performances of LSBs. In this study, a template method was used to prepare the Co nanoparticle-embedded N-doped hierarchical porous carbon network (Co-NHPC) with good adsorption and catalytic conversion ability of LiPSs. The results show that Co-NHPC provides a high initial specific capacity of 1478.6 mA h g^{-1} at 0.2 C. Even after 500 cycles, Co-NHPC maintains good reversible capacities of 674.9 and 451.6 mA h g^{-1} at 1 and 5 C, respectively.

Keywords: lithium-sulfur battery, cathode, hierarchical structure, porous carbon

INTRODUCTION

Lithium-sulfur batteries (LSBs) offer a high theoretical capacity of 1675 mA h g^{-1} and an energy density of up to 2600 W h kg^{-1}, which have been considered one of the most promising energy storage systems [1–5]. However, the practical implementation of LSBs encounters obstacles, including low conductivity of sulfur species [6,7], large volume expansion of 80% during discharge due to the transformation of S into Li_2S_2 and Li_2S, and the shuttle effect of lithium polysulfides (LiPSs) [8–10]. This usually causes a considerable degradation in their capacity and a reduction in their cycle life. Therefore, exploring a cathode with good conductivity for electron transfer and stable porous micro/nanostructures is critical to efficiently accommodate volume variation and accelerate catalytic sulfur species conversion.

A series of carbon materials, such as graphene [11,12], carbon nanotubes [13,14], carbon fibers [15], and porous carbon [16–18], have been reported since Nazar and coworkers [19] demonstrated excellent LSBs performance by confining sulfur in mesoporous CMK-3. Porous carbon with high specific surface area, good electrical conductivity, and adjustable pore size can not only improve the conductivity of porous carbon but also promote electrolyte penetration, Li^+ migration, and sulfur/polysulfide adsorption [20,21]. For example, the mesoporous core–shell carbon cathode enhanced the adsorption of LiPSs and accelerated their reaction kinetics, retaining a specific capacity of 837.0 mA h g^{-1} at 0.5 C, even after 200 cycles [22]. However, the severe shuttle effect due to the nonpolar surface of carbon causes unsatisfactory LSBs cycle performance [23–26]. N doping has been effectively used for improving the chemisorption capacity of LiPSs by interacting with the terminal Li^+ of LiPSs, thereby favoring the fixation of polysulfides to enhance their charge/discharge stability [27–29]. However, this strategy is not sufficient to accelerate the redox kinetics for avoiding LiPSs accumulation. Additionally, introducing transition metal (e.g., Fe, Co, and Ni) components into the carbon structures contributed to LiPSs adsorption by forming metal–S bonds with LiPSs [30–32]. Moreover, the transition metal could promote electron transfer, facilitating the catalytic reduction of LiPSs [33–35].

In this study, we used g-C_3N_4 as a template for preparing Co nanoparticles (NPs)-embedded N-doped hierarchical porous carbon network (Co-NHPC) as the sulfur carrier for LSBs. g-C_3N_4 acts as the N source and leaves cavities *via* pyrolysis, while dopamine hydrochloride encapsulated on g-C_3N_4 serves as the main carbon source and accommodates Co ions. Finally, Co NPs could be *in situ* derived and embedded in the carbon network to form a stable hybrid structure. The detailed characterization shows that Co-NHPC has a high initial capacity, good rate, and reversible capacities; therefore, the material could be used as a high-performance cathode for LSBs.

EXPERIMENTAL SECTION

Preparation of g-C_3N_4

Melamine (10 g) was placed in an alumina crucible with a lid and kept at 550°C for 4 h under an air atmosphere at a heating rate of 2.3°C min^{-1}. After cooling to room temperature, the plates were heated again at a rate of 10°C min^{-1} and kept at 520°C for 4 h in a crucible without a lid. The as-obtained g-C_3N_4 was then subjected to ball milling for another 4 h.

Preparation of NHPC, Co-C, and Co-NHPC

g-C_3N_4 (0.5 g) was uniformly dispersed in a solution of deionized water (94 mL) and ethanol (36 mL) and then sonicated for 1 h (labeled as solution A). Dopamine hydrochloride (0.5 g) and cobalt acetylacetone (28.5 mg) were dissolved in a solution of deionized water (6 mL) and ethanol (4 mL) and labeled as solution B. Solution B was then poured into solution A under stirring. The resulting mixture was stirred for 12 h at room temperature, and then centrifuged and washed with water to obtain $Co(acac)_2$@PDA@g-C_3N_4; further, it was annealed at

Key Laboratory of Bio-inspired Smart Interfacial Science and Technology of Ministry of Education, School of Chemistry, Beihang University, Beijing 100191, China
* Corresponding authors (emails: liudp@buaa.edu.cn (Liu D); jade@buaa.edu.cn (Zhang Y))

900°C for 4 h under Ar atmosphere, and treated with 1 mol L^{-1} HCl for 24 h at 60°C followed by drying in a vacuum oven to obtain Co-NHPC. Similarly, NHPC and Co NP-embedded carbon spheres (Co-C) were prepared without adding cobalt acetylacetonate or g-C_3N_4.

Preparation of sulfur-loaded cathodes

Sulfur powder was thoroughly mixed with the catalytic material in a mass ratio of 4:1. The mixture was dissolved in a carbon disulfide solution, dried *via* ultrasonic evaporation, transferred to an Ar-filled hydrothermal steel reactor, and kept at 155°C for 16 h. Thus, three cathode materials were obtained.

Characterizations

The powder X-ray diffraction (XRD) patterns were acquired using a D8 ADVANCE (Brooke (Beijing) Technology Company Limited) with Cu-Kα radiation (λ = 0.15418 nm). Morphology and elemental mapping of samples were collected using a JSM-7500F scanning electron microscope (SEM) and an FEI Titan Themis G3 transmission electron microscope (TEM). Raman spectroscopy was performed on a Renishaw inVia spectrometer in the wavenumber range of 500–2000 cm^{-1} with 532 nm laser excitation under ambient conditions. N_2 adsorption/desorption isotherms and specific surface area data of the samples were investigated at 77 K on a MaiKe ASAP2460. X-ray photoelectron spectroscopy (XPS) was performed on an ESCALab250Xi photoelectron spectrometer with Al-Kα X-ray radiation as the excitation source to determine the surface chemical states of the samples. Elemental analysis on Co was performed on a Thermo Fisher Scientific iCAP RQ inductively coupled plasma mass spectrometer (ICP-MS).

Synthesis of S-Al cathodes

The S-Al cathode was prepared by dissolving 70 wt% cathode materials, 20 wt% carbon black, and 10 wt% polyvinylidene fluoride (PVDF) in *N*-methyl-2-pyrrolidone (NMP). The homogeneously mixed slurry was pasted on an Al foil current collector and dried under vacuum at 60°C for 16 h. The as-obtained cathode sheets were stamped into small disks with the diameter of 12 mm, each containing approximately 1 mg cm^{-2} of sulfur.

Assembly and electrochemical measurements of LSBs

The cathode sheet, diaphragm, and lithium sheet as the counter electrode were successively put into the CR2025 cell shell for LSB assembly. The electrolyte was composed of 1 mol L^{-1} lithium di(trifluoromethane) sulfonimide (LiTFSI) dissolved in a mixture of 1,3-dioxyalkane (DOL) and 1,2-dimethoxyethane (DME) (v/v = 1/1) with 1 wt% $LiNO_3$ as the additive. The electrolyte/sulfur (E/S) ratios were approximately 17.0 and 8.1 μL mg^{-1} for coin and high-load sulfur coin cells, respectively. Constant current charge/discharge curves and rate/cycle performance were collected on a Land CT2001A battery test system with a voltage range from 1.7 to 2.8 V (for Li^+/Li). Cyclic voltammetry (CV) was performed at a scan rate of 0.1 mV s^{-1}, and the electrochemical impedance spectroscopy (EIS) was performed over a frequency range of 100 kHz to 100 mHz using a VSP electrochemical workstation.

Symmetrical cell assembly and measurements

First, a solution of 0.5 mol L^{-1} Li_2S_6 was obtained by adding sulfur and Li_2S with a molar ratio of 5:1 to DME and DOL (v/v = 1/1). The electrodes of the symmetrical cell were prepared in the absence of sulfur. The active material was mixed with NMP in a molar ratio of 9:1, coated on an Al foil, and punched into disks with a diameter of 12 mm. Symmetric CR2025 coin cells were assembled with 0.5 mol L^{-1} Li_2S_6 electrolyte (20 μL) and 1 mol L^{-1} LiTFSI dissolved in 20 μL of DOL/DME (v/v = 1/1). Two identical electrodes (mass loading of active materials of approximately 1.0 mg cm^{-2}) served as the working and counter electrodes. CV tests of symmetric cells were performed at a scan rate of 30 mV s^{-1} with the voltage ranging from −0.8 to 0.8 V at 25°C.

Nucleation of Li_2S on different reactive surfaces

To investigate the liquid–solid transition kinetics, we used different materials as the working cathodes and lithium metal as the anodes and assembled them into coin cells for the nucleation test of Li_2S. The electrolyte of the Li_2S_8 solution (0.5 mol L^{-1}) was prepared by mixing a stoichiometry of 1:7 for Li_2S and sulfur powder in DME and DOL (v/v = 1/1) and then underwent strong magnetic stirring for 12 h at 60°C. Li_2S_8 (25 μL, 0.5 mol L^{-1}) was dropped onto the cathode side, and 25 μL of LiTFSI electrolyte was added to the anode side. The assembled cells were first discharged galvanostatically at 0.112 mA to 2.09 V and then discharged potentiostatically at 2.08 V for Li_2S nucleation and growth. The potentiostatic discharge was terminated when the current fell below 10^{-5} A.

Visualized adsorption experiments

NHPC, Co-C, and Co-NHPC powders (10 mg) were added simultaneously to a 5 mL Li_2S_6 solution (5 mol L^{-1}) inside a glove box. The color changes observed in the three solutions were recorded and compared with those of the pure Li_2S_6 solution. The concentration of the adsorbed slag solution was determined using ultraviolet-visible (UV-vis) spectrophotometry.

Shuttle current measurement

$LiNO_3$-free electrolyte was used for the shuttle current measurement. Cells were first discharged/charged for two cycles and then charged at a constant current of 0.2 C until the voltage reached 2.80 V. The battery was then discharged to 2.38 V and switched to the constant potential mode. After about 3×10^4 s, the potentiostatic current was stabilized at a steady state as the shuttle current.

LSV measurement

Linear sweep voltammetry (LSV) experiments were used to investigate the Li_2S oxidation activity of different materials in a three-electrode structure. The cells were composed of modified "carbon glass" disks (3 mm in diameter) with the as-prepared composites as the working electrode, an Ag/AgCl electrode as the reference, a platinum sheet as the counter electrode, and 0.1 mol L^{-1} Li_2S/methanol solution as the electrolyte. LSV was measured at a scan rate of 5 mV s^{-1} between −0.8 and −0.1 V.

RESULTS AND DISCUSSION

Scheme 1 schematically shows the synthetic process of Co-NHPC. First, g-C_3N_4 was ground into particles with a size of 0.1–1.5 μm by ball milling (Fig. S1). The as-obtained g-C_3N_4 was then coated by dopamine hydrochloride with a thickness of

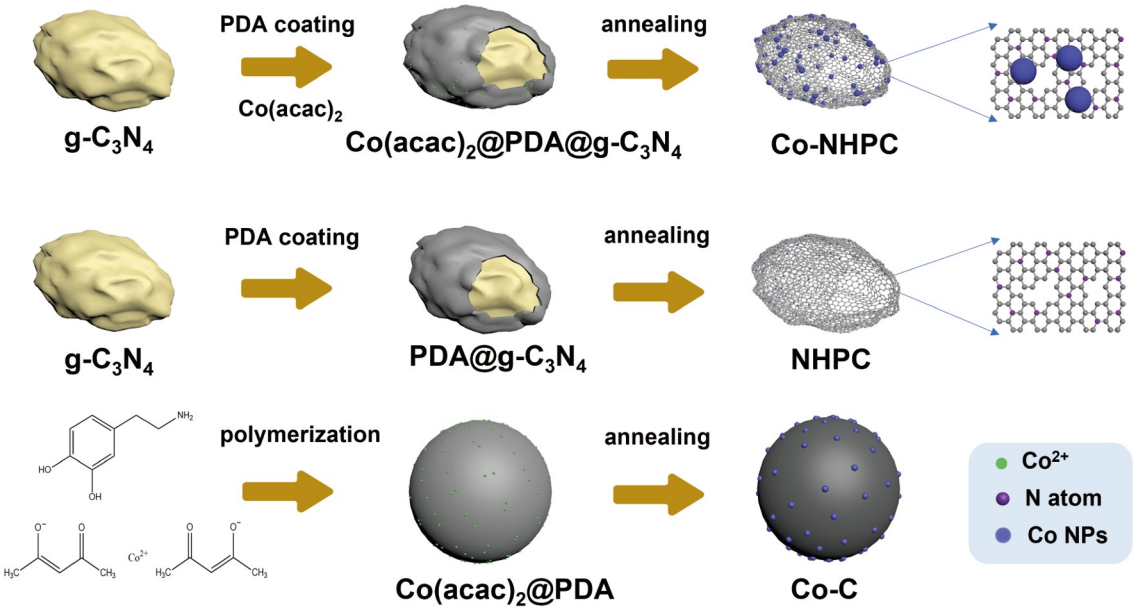

Scheme 1 Schematic of Co-NHPC synthesis.

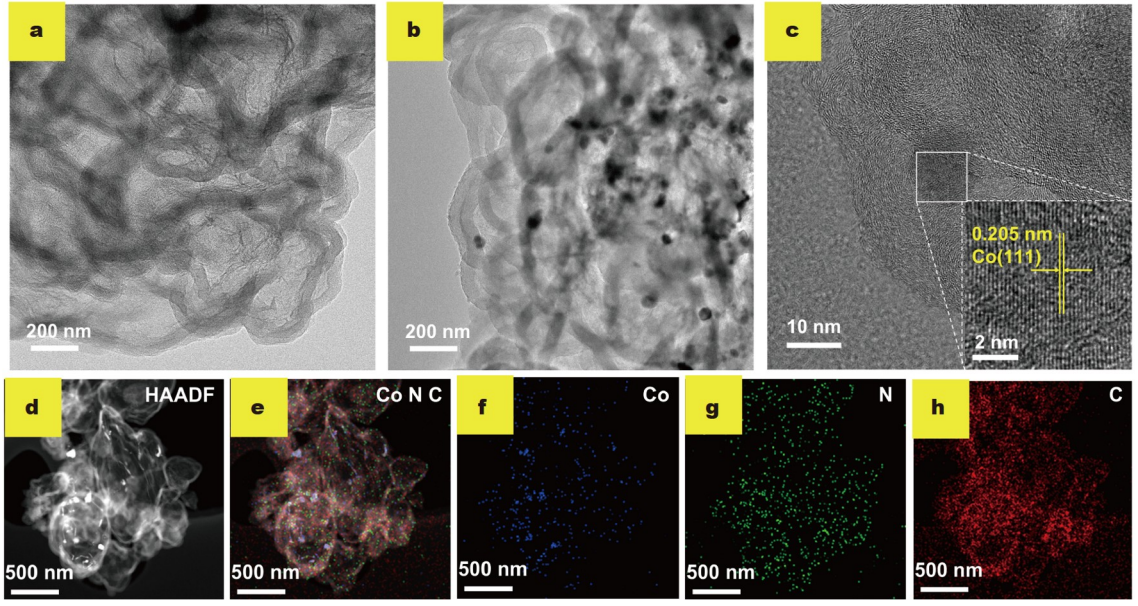

Figure 1 TEM images of (a) NHPC and (b) Co-NHPC after pickling; (c) the corresponding high-resolution TEM image and (d–h) elemental mapping analysis of Co-NHPC.

20 nm in alkaline. After annealing, NHPC was obtained, as shown in Fig. 1a and Fig. S2. Removing g-C_3N_4 would result in significant hollow structures and leave a considerable amount of N elements that are uniformly distributed in the carbon network verified by element mapping analysis (Fig. S3). Co-NHPC was successfully synthesized after cobalt acetylacetone was introduced during the coating process. The TEM (Fig. 1b) and SEM (Fig. S4) images of Co-NHPC show that the vesicular structure could be well preserved after introducing Co salts, and the wall thickness of vesicles remains almost unchanged. The residue Co NPs with an average size of 12 nm after pickling are protected by a carbon layer (Fig. 1c and Fig. S5). The lattice fringe spacing of 0.205 nm corresponds well to the Co (111) plane (Fig. 1c, inset). The elemental mapping analysis in Fig. 1d–h shows the existence of Co NPs and the homogeneous distribution of doped N-heteroatoms. In contrast, in the absence of g-C_3N_4, only Co NP-embedded carbon spheres (Co-C) could be obtained due to the self-polymerization of dopamine hydrochloride into a sphere-like precursor. As shown in Fig. S6, Co-C solid spheres show an approximate size of 200–800 nm. Co contents in Co-NHPC and Co-C were determined using ICP-MS as 4.7 and 6.0 wt%, respectively.

The shadow part in the XRD patterns (Fig. 2a) illustrates the typical signals of amorphous carbon. For Co-NHPC and Co-C, the diffraction peaks at approximately 44.5°, 52.0°, and 76.0° correspond to Co metal (JCPDS no. 15-0806). In the Raman

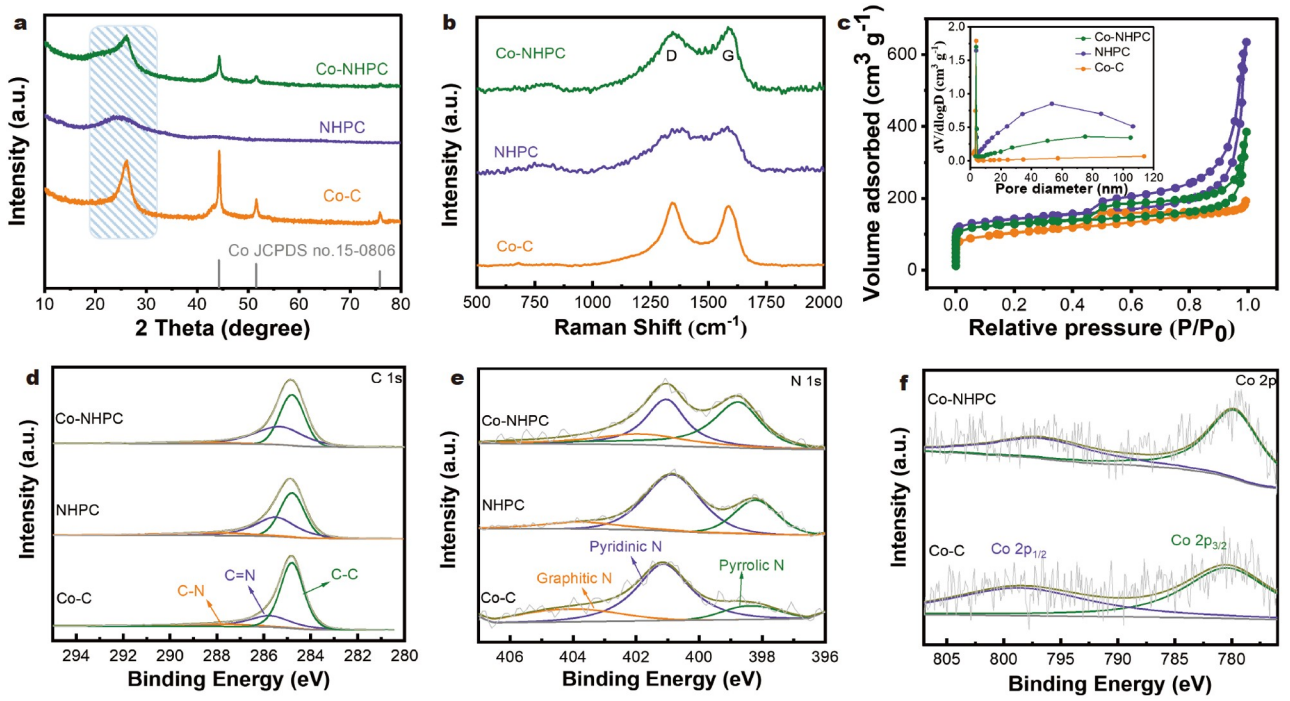

Figure 2 (a) XRD patterns, (b) Raman spectra, (c) N_2 adsorption/desorption isotherms (inset: pore size distribution), and XPS spectra of (d) C 1s, (e) N 1s, and (f) Co 2p of Co-NHPC, NHPC, and Co-C.

spectra (Fig. 2b), the D band (1340 cm^{-1}) corresponds to the defective carbon, whereas the G band (1590 cm^{-1}) corresponds to the in-plane stretching vibration of the sp^2 hybridization of carbon atoms [36]. The relative intensity ratios (I_D/I_G) of Co-NHPC, NHPC, and Co-C are 0.85, 0.98, and 1.06, respectively, indicating the higher degree of graphitization for Co-NHPC, which is more conducive to electron transfer.

According to the IUPAC classification, Fig. 2c shows an obvious combination of type I and IV isotherms in the N_2 isothermal adsorption/desorption curves. Each of the three samples has intense adsorption at low relative pressures (<0.05), corresponding to abundant micropores and clear hysteresis loops at high relative pressures (0.4–1.0), corresponding to mesoporous structures. Moreover, the pore size distribution (Fig. 2c, inset) reflects the porous hierarchical structures of Co-NHPC and NHPC. Pyrolysis of g-C_3N_4 leaves a large Brunauer–Emmett–Teller surface area and pore volume (Table S1). As reported in a previous study [37], the abundant porous structure could provide sufficient space to host sulfur and suitable pore size distribution and large surface area ensure effective contact between the active materials and sulfur species. As observed from the fitted XPS spectra (Fig. 2d) of C 1s, the strongest peaks are observed at 284.8 eV, corresponding to sp^2 carbon, and 285.5 and 287.9 eV, corresponding to the C=N and C–N bonds, respectively [30]. In the N 1s spectra (Fig. 2e), the peaks at 398.2, 400.9, and 403.3 eV correspond to pyrrolic N, pyridinic N, and graphitic N, respectively [38]. Additionally, the proportion of pyrrolic N in Co-NHPC is higher than that in NHPC and Co-C; this is because the pyrrolic N in Co-NHPC binds more strongly to LiPSs than the other two N atom types [38]. Fig. 2f shows two characteristic peaks at 780.3 and 799.9 eV in the high-resolution Co 2p spectra, corresponding to Co metal [39]. In the SEM (Fig. S7) and TEM images (Fig. S8a–c), the morphologies of Co-NHPC and NHPC remain unchanged after dissolving sulfur. Additionally, the elemental mapping (Fig. S8d–i) of Co, N, C, and S for Co-NHPC confirms the uniform sulfur distribution, indicating the successful loading of sulfur into the pores. In contrast, large agglomerated sulfur particles appear on the Co-C surface (Fig. S9). Each of the three cathodes shows the characteristic XRD peaks of sulfur (Fig. S10), and Co-NHPC has a sulfur content of 80.7%, as evidenced by thermogravimetric analysis (Fig. S11).

Fig. 3a shows that Co-NHPC exhibits a high initial specific capacity of 1478.6 mA h g^{-1} at 0.2 C (1 C = 1675.0 mA h g^{-1}), corresponding to 88.3% of sulfur utilization. In contrast, the initial discharge-specific capacities of NHPC and Co-C are 1102.1 and 1138.3 mA h g^{-1}, corresponding to 65.8% and 68.0% of sulfur utilization, respectively. After 100 cycles, the reversible capacities of NHPC and Co-C decrease to only 752.5 and 644.4 mA h g^{-1}, significantly lower than that of Co-NHPC (990.9 mA h g^{-1}). As shown in Fig. 3b, Co-NHPC demonstrates higher reversible specific capacities at various rate capacities than NHPC and Co-C, whose average capacities reach 1189.1, 998.9, 900.8, 841.7, and 771.0 mA h g^{-1} when the current density increases from 0.1 to 0.2, 0.5, 1, and 2 C, respectively. Moreover, Co-NHPC could rapidly recover its specific capacity to 948.2 mA h g^{-1} from 2 to 0.2 C, indicating good reversibility. In the constant current charge/discharge profiles of Co-NHPC (Fig. 3c), the discharge curve shows two relatively flat potential plateaus, and the voltage gap widens slightly as the discharge rate increases. The lower overpotential of Co-NHPC reflects its better kinetic response (Fig. S12).

Co-NHPC exhibits a higher initial discharge-specific capacity of 1084.0 mA h g^{-1} than NHPC (944.7 mA h g^{-1}) and Co-C (812.2 mA h g^{-1}) at 1 C (Fig. 3d). After 500 cycles, its reversible specific capacity is maintained at 674.9 mA h g^{-1} with a minimal

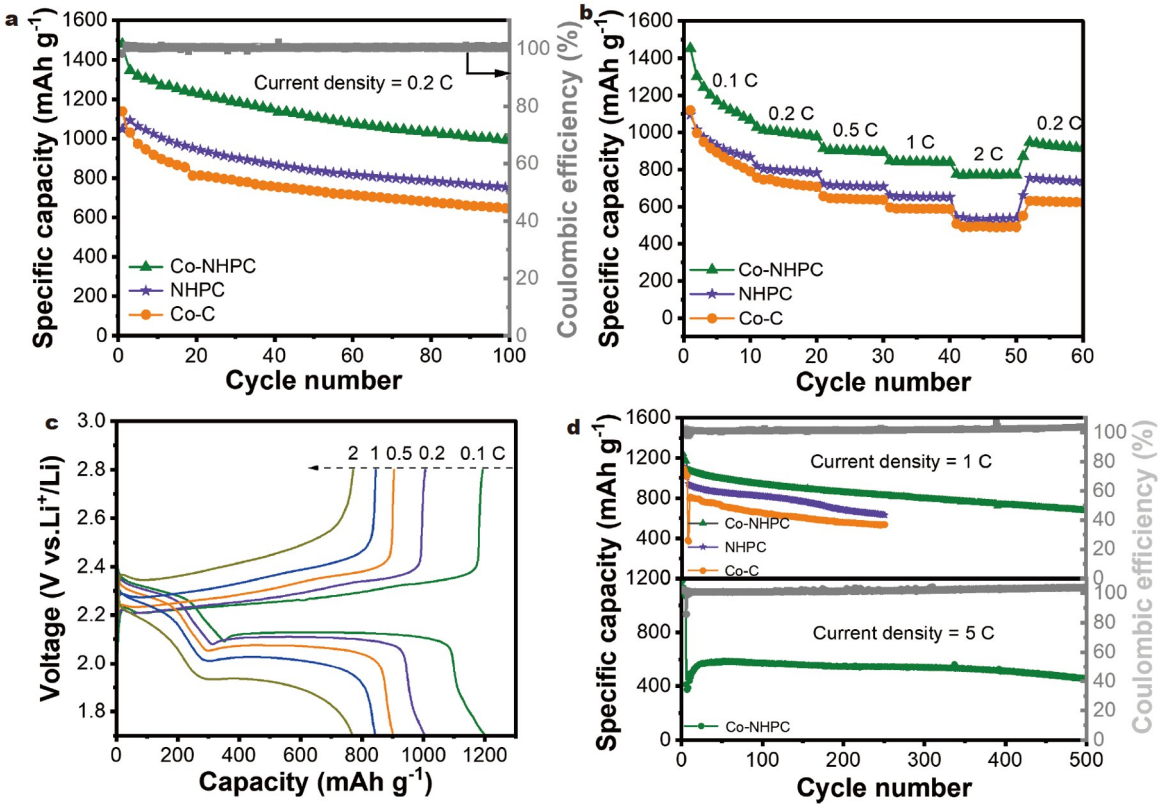

Figure 3 (a) Cycle performances at 0.2 C and (b) rate performances of Co-NHPC, NHPC, and Co-C at different current densities; (c) charge/discharge curves of Co-NHPC; (d) cycle performances of different samples at 1 and 5 C.

capacity decay of only 0.075% per cycle. Even at a high current density of 5 C, its cycle stability remains well, and the discharge-specific capacity of Co-NHPC increases from 373.6 to 590.0 mA h g^{-1} after activation. Additionally, its reversible specific capacity remains constant at 451.6 mA h g^{-1} after 500 cycles with only a small decay of 0.047% per cycle. For high-sulfur-loading tests (Fig. S13), the Co-NHPC cathode with a sulfur loading of 3.7 mg and a liquid-to-mass ratio of 8.1 μL mg^{-1} shows an initial specific capacity of 1021.0 mA h g^{-1} at a current density of 0.1 C. Furthermore, it maintains a reversible specific capacity of 831.3 mA h g^{-1} after 100 cycles. Thus, the specific surface area should not be considered as the decisive factor for exhibiting high catalytic performance of Co-NHPC, and Co NPs in Co-NHPC are found to contribute much to the catalytic activity [33].

Further electrochemical tests were conducted to elucidate the contribution of porous structure and Co components to sulfur redox kinetics. In the CV curves (Fig. 4a), Peak I (2.24 V) and Peak II (1.99 V) of Co-NHPC correspond to the multiple reduction processes of S_8 to LiPSs and further reduction to insoluble Li_2S/Li_2S_2, respectively, corresponding to the dual plateau of the discharge process. Peak III (2.38 V) corresponds to the oxidation of Li_2S/Li_2S_2 into LiPSs and sulfur during charge. Co-NHPC exhibits a stronger current response with a positive reduction peak shift and a negative oxidation peak shift than NHPC and Co-C. Table S2 presents the EIS parameters from the equivalent circuit (R_s, R_{ct}, constant phase elements (CPEs), and Warburg). It confirms that the charge transfer resistance is reduced after introducing Co (Fig. 4b). The Li_2S_6-free cells failed in the CV test of symmetrical cells (Fig. 4c). However, after adding Li_2S_6, the current density was strongly dependent on the cathodes. Co-NHPC possesses the best performance under the same conditions because of its highest catalytic activity toward LiPSs.

Furthermore, an equal amount of samples was added to a 5-mmol L^{-1} Li_2S_6 solution to evaluate the adsorption capacity of Co-NHPC, NHPC, Co-C, and carbon black toward LiPSs. As shown in Fig. S14, the yellow Li_2S_6 solution containing Co-NHPC quickly turns colorless, while others fade slowly to different extents; this is consistent with the findings from UV-vis analyses (Fig. 4d). The lowest current of Co-NHPC demonstrates its best ability to inhibit the shuttle effect (Fig. 4e). Meanwhile, the corresponding anode of Co-NHPC is barely corroded, and its separator is almost colorless (Fig. 4e, inset). SEM (Fig. S15) and TEM (Fig. S16a, b) images indicate that Co-NHPC could maintain its morphology well after cycling, and its surface is free of large sulfur particles different from the NHPC and Co-C surfaces. This indicates that sulfur has been well restricted in the pores of Co-NHPC, as observed from the elemental mapping analysis (Fig. S16c–h), suggesting its excellent sulfur-loading capacity and structural stability. As displayed in the LSV curves (Fig. 4f), the highest current response and smallest Tafel slope of 20.1 mV dec^{-1} for Co-NHPC (Fig. S17) demonstrate its good activity for Li_2S catalytic oxidation. Meanwhile, the Li_2S nucleation experiments (Fig. 4g–i) show that Co-NHPC has the largest deposition capacity (244.7 mA h g^{-1}), the lowest energy barrier for Li_2S nucleation, and the fastest reduction kinetics for LiPSs during the surface

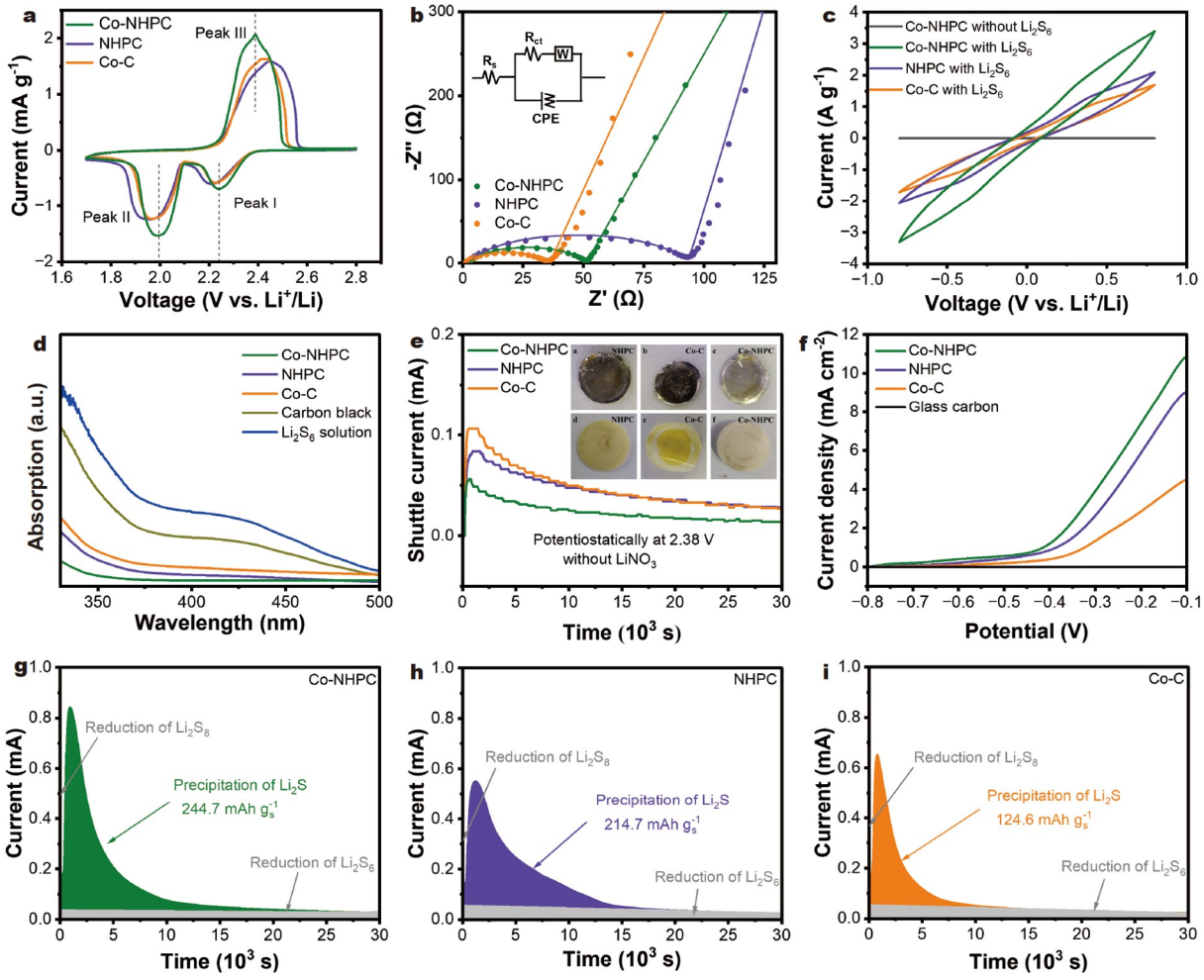

Figure 4 (a) CV curves of asymmetric cells; (b) EIS curves of LSBs; (c) CV curves of Li_2S_6 and Li_2S_6-free symmetrical cells; (d) UV-vis spectra; (e) shuttle current tests of Li_2S_6 solution after adsorption (inset: photographs of the disassembled cells after 500 cycles at 1 C); (f) LSV profiles of the samples; (g–i) potentiostatic discharge profiles of Li_2S nucleation for Co-NHPC, NHPC and Co-C.

phase transition of sulfur species.

CONCLUSION

In this study, Co-NHPC was fabricated using a simple template method, exhibiting unique advantages in LSB applications. The large porous structure generated by the pyrolysis of g-C_3N_4 enables the cathode to accommodate a sufficient amount of S, which effectively mitigates its volume expansion during charge/discharge. The large specific surface area and suitable pore size distribution of Co-NHPC promote electrolyte diffusion and expand the electrode–electrolyte surface contact. Additionally, N doping and Co NP embedding effectively enhance the adsorption and catalytic conversion abilities of liquid LiPSs. Benefiting from these advantages, Co-NHPC shows a high initial reversible specific capacity of 1478.6 mA h g^{-1} at 0.2 C. After 500 cycles, the reversible specific capacities of 674.9 and 451.6 mA h g^{-1} are maintained at higher rates of 1 and 5 C, respectively. Sufficient inhibition of shuttle effects indicates that a reasonable structural design strategy can inspire high-performance LSBs.

Received 28 July 2023; accepted 18 October 2023; published online 24 November 2023

1 Seh ZW, Sun Y, Zhang Q, *et al.* Designing high-energy lithium-sulfur batteries. Chem Soc Rev, 2016, 45: 5605–5634
2 Yang Y, Zheng G, Cui Y. Nanostructured sulfur cathodes. Chem Soc Rev, 2013, 42: 3018–3032
3 Peng HJ, Huang JQ, Cheng XB, *et al.* Review on high-loading and high-energy lithium-sulfur batteries. Adv Energy Mater, 2017, 7: 1700260
4 Shi M, Liu Z, Zhang S, *et al.* A Mott–Schottky heterogeneous layer for Li-S batteries: Enabling both high stability and commercial-sulfur utilization. Adv Energy Mater, 2022, 12: 2103657
5 Lu W, Wang Z, Sun G, *et al.* Anchoring polysulfide with artificial solid electrolyte interphase for dendrite-free and low N/P ratio Li-S batteries. J Energy Chem, 2023, 80: 32–39
6 Ding B, Wang J, Fan Z, *et al.* Solid-state lithium-sulfur batteries: Advances, challenges and perspectives. Mater Today, 2020, 40: 114–131
7 Zhang E, Hu X, Meng L, *et al.* Single-atom yttrium engineering Janus electrode for rechargeable Na-S batteries. J Am Chem Soc, 2022, 144: 18995–19007
8 Kang Q, Li Y, Zhuang Z, *et al.* Dielectric polymer based electrolytes for high-performance all-solid-state lithium metal batteries. J Energy Chem, 2022, 69: 194–204
9 Sun H, Xu GL, Xu YF, *et al.* A composite material of uniformly dispersed sulfur on reduced graphene oxide: Aqueous one-pot synthesis, characterization and excellent performance as the cathode in rechargeable lithium-sulfur batteries. Nano Res, 2012, 5: 726–738
10 Lei J, Liu T, Chen J, *et al.* Exploring and understanding the roles of

Li_2S_n and the strategies to beyond present Li-S batteries. Chem, 2020, 6: 2533–2557
11 Tantis I, Bakandritsos A, Zaoralová D, *et al.* Covalently interlinked graphene sheets with sulfur-chains enable superior lithium-sulfur battery cathodes at full-mass level. Adv Funct Mater, 2021, 31: 2101326
12 Zhe R, Zhu T, Wei X, *et al.* Graphene oxide wrapped hollow mesoporous carbon spheres as a dynamically bipolar host for lithium-sulfur batteries. J Mater Chem A, 2022, 10: 24422–24433
13 Jiang J, Fan Q, Zheng Z, *et al.* The dual functions of defect-rich carbon nanotubes as both conductive matrix and efficient mediator for Li-S batteries. Small, 2021, 17: 2103535
14 Li Y, Wang X, Sun M, *et al.* CoSe nanoparticle embedded B,N-codoped carbon nanotube array as a dual-functional host for a high-performance Li-S full battery. ACS Nano, 2022, 16: 17008–17020
15 Shih HJ, Chang JY, Cho CS, *et al.* Nano-carbon-fiber-penetrated sulfur crystals as potential cathode active material for high-performance lithium-sulfur batteries. Carbon, 2020, 159: 401–411
16 Thangavel R, Kannan AG, Ponraj R, *et al.* Cinnamon-derived hierarchically porous carbon as an effective lithium polysulfide reservoir in lithium-sulfur batteries. Nanomaterials, 2020, 10: 1220
17 Wei Y, Tao Y, Zhang C, *et al.* Layered carbide-derived carbon with hierarchically porous structure for high rate lithium-sulfur batteries. Electrochim Acta, 2016, 188: 385–392
18 Zhang C, Wu HB, Yuan C, *et al.* Confining sulfur in double-shelled hollow carbon spheres for lithium-sulfur batteries. Angew Chem Int Ed, 2012, 51: 9592–9595
19 Ji X, Lee KT, Nazar LF. A highly ordered nanostructured carbon-sulphur cathode for lithium-sulphur batteries. Nat Mater, 2009, 8: 500–506
20 Xiang Y, Lu L, Kottapalli AGP, *et al.* Status and perspectives of hierarchical porous carbon materials in terms of high-performance lithium-sulfur batteries. Carbon Energy, 2022, 4: 346–398
21 Zhang L, Wang Y, Niu Z, *et al.* Advanced nanostructured carbon-based materials for rechargeable lithium-sulfur batteries. Carbon, 2019, 141: 400–416
22 Li Z, Jiang Y, Yuan L, *et al.* A highly ordered meso@microporous carbon-supported sulfur@smaller sulfur core–shell structured cathode for Li-S batteries. ACS Nano, 2014, 8: 9295–9303
23 Du Z, Chen X, Hu W, *et al.* Cobalt in nitrogen-doped graphene as single-atom catalyst for high-sulfur content lithium-sulfur batteries. J Am Chem Soc, 2019, 141: 3977–3985
24 Zhou W, Yu Y, Chen H, *et al.* Yolk–shell structure of polyaniline-coated sulfur for lithium-sulfur batteries. J Am Chem Soc, 2013, 135: 16736–16743
25 Wang J, Han W. A review of heteroatom doped materials for advanced lithium-sulfur batteries. Adv Funct Mater, 2021, 32: 2107166
26 Wang Z, Feng M, Sun H, *et al.* Constructing metal-free and cost-effective multifunctional separator for high-performance lithium-sulfur batteries. Nano Energy, 2019, 59: 390–398
27 Lee JS, Manthiram A. Hydroxylated N-doped carbon nanotube-sulfur composites as cathodes for high-performance lithium-sulfur batteries. J Power Sources, 2017, 343: 54–59
28 Guo D, Zhang X, Liu M, *et al.* Single Mo-N_4 atomic sites anchored on N-doped carbon nanoflowers as sulfur host with multiple immobilization and catalytic effects for high-performance lithium-sulfur batteries. Adv Funct Mater, 2022, 32: 2204458
29 Li F, Su Y, Zhao J. Shuttle inhibition by chemical adsorption of lithium polysulfides in B and N Co-doped graphene for Li-S batteries. Phys Chem Chem Phys, 2016, 18: 25241–25248
30 Zuo X, Zhen M, Liu D, *et al.* A multifunctional catalytic interlayer for propelling solid–solid conversion kinetics of Li_2S_2 to Li_2S in lithium-sulfur batteries. Adv Funct Mater, 2023, 33: 2214206
31 Hu Y, Cheng C, Yan T, *et al.* Catalyzing polysulfide redox conversion for promoting the electrochemical performance of lithium-sulfur batteries by CoFe alloy. Chem Eng J, 2021, 421: 129997
32 Huang J, Leng K, Cen Z, *et al.* Cobalt-decorated carbon nanotube bottlebrushes for boosting polysulfide conversion in lithium-sulfur batteries. Sci China Mater, 2023, 66: 1747–1756
33 Wang Y, Zhou Y, Feng Y, *et al.* Synergistic electronic and pore structure modulation in open carbon nanocages enabling efficient electrocatalytic production of H_2O_2 in acidic medium. Adv Funct Mater, 2022, 32: 2110734
34 Yuan C, Zeng P, Cheng C, *et al.* Boosting the rate performance of Li-S batteries *via* highly dispersed cobalt nanoparticles embedded into nitrogen-doped hierarchical porous carbon. CCS Chem, 2022, 4: 2829–2841
35 Xu Y, Tu W, Zhang B, *et al.* Nickel nanoparticles encapsulated in few-layer nitrogen-doped graphene derived from metal-organic frameworks as efficient bifunctional electrocatalysts for overall water splitting. Adv Mater, 2017, 29: 1605957
36 Li B, Xi B, Feng Z, *et al.* Hierarchical porous nanosheets constructed by graphene-coated, interconnected TiO_2 nanoparticles for ultrafast sodium storage. Adv Mater, 2018, 30: 1705788
37 Song J, Xu T, Gordin ML, *et al.* Nitrogen-doped mesoporous carbon promoted chemical adsorption of sulfur and fabrication of high-areal-capacity sulfur cathode with exceptional cycling stability for lithium-sulfur batteries. Adv Funct Mater, 2014, 24: 1243–1250
38 Wang R, Yang J, Chen X, *et al.* Highly dispersed cobalt clusters in nitrogen-doped porous carbon enable multiple effects for high-performance Li–S battery. Adv Energy Mater, 2020, 10: 1903550
39 Liu S, Li J, Yan X, *et al.* Superhierarchical cobalt-embedded nitrogen-doped porous carbon nanosheets as two-in-one hosts for high-performance lithium-sulfur batteries. Adv Mater, 2018, 30: 1706895

Acknowledgements This work was financially supported by the National Natural Science Foundation of China (51925202 and 51972008).

Author contributions Fu L and Zuo X conceived and supervised the experiments; Fu L prepared the materials and performed the property characterizations; Fu Z and Yu H carried out materials characterization; Fu L wrote the manuscript with help from all authors. All authors contributed to the general discussion.

Conflict of interest The authors declare that they have no conflict of interest.

Supplementary information Supporting data are available in the online version of the paper.

Lichao Fu is currently a graduate student at the School of Chemistry, Beihang University. His research interest is the design and performance of cathode materials for lithium-sulfur batteries.

Dapeng Liu received his PhD degree from Jilin University in 2008. During 2008–2012, he finished his postdoctoral research and worked as an associate professor at Changchun Institute of Applied Chemistry, Chinese Academy of Sciences. Then, he moved to the School of Chemistry, Beihang University in 2013. His research mainly focuses on rare earth nanostructures for energy materials and catalytic applications.

Yu Zhang received his PhD degree from Jilin University in 2007. Then, he worked as a New Energy and Industrial Technology Development Organization fellow at Hiroshima University, Japan. He joined Beihang University in 2013 and is now a full professor at the School of Chemistry. His interest is focused on advanced energy materials, especially on optimizing electrode structures in the Li-air and Li/Na-ion battery fields.

钴纳米颗粒嵌入的分级多孔碳正极用于高性能锂硫电池

付莅超, 刘大鹏*, 左鑫涛, 于浩涵, 付泽瑞, 张瑜*

摘要 锂硫电池理论能量密度大、成本低廉，被认为是最有前景的电化学储能系统之一. 然而，硫和放电产物硫化锂的低电导率，充放电时的体积膨胀，以及多硫化锂的穿梭效应严重影响了其可逆容量和循环性能. 本文采用了一种简单的模板法制备了Co纳米颗粒嵌入的分级多孔碳网络(Co-NHPC). 通过合理结构设计，以及原位生成的Co纳米颗粒的嵌入，Co-NHPC表现出很强的对LiPSs的吸附和催化转化能力. 结果表明，Co-NHPC在0.2 C时的初始可逆容量为1478.6 mA h g^{-1}，经过500次循环后，在1和5 C下仍可分别保留674.9和451.6 mA h g^{-1}的可逆容量.

